Tunable multiphoton Rabi oscillations in an electronic spin system

S. Bertaina,[1,2,*] N. Groll,[2,†] L. Chen,[2,3] and I. Chiorescu[2,‡]

[1]*Institut Matériaux Microélectronique et Nanosciences de Provence, Unité Mixte de Recherche No. 6242 associée au Centre National de la Recherche Scientifique and Aix-Marseille Université, Faculté des Sciences et Techniques, Avenue Escadrille Normandie Niemen, Case 142, F-13397 Marseille Cedex, France*

[2]*Department of Physics and The National High Magnetic Field Laboratory, Florida State University, Tallahassee, Florida 32310, USA*

[3]*Department of Chemistry and Chemical Biology, Cornell University, Ithaca, New York 14853-1301, USA*

(Received 7 June 2011; revised manuscript received 29 July 2011; published 20 October 2011)

We report on multiphoton Rabi oscillations and controlled tuning of a multilevel system at room temperature ($S = 5/2$ for Mn^{2+}:MgO) in and out of a quasiharmonic level configuration. The anisotropy is much smaller than the Zeeman splittings, e.g., the six-level scheme shows only a small deviation from an equidistant diagram. This allows us to tune the spin dynamics by compensating for the cubic anisotropy with either a precise static-field orientation or a microwave field intensity. Using the rotating-frame approximation, the experiments are explained very well by both an analytical model and a generalized numerical model. The calculated multiphoton Rabi frequencies are in excellent agreement with the experimental data.

DOI: 10.1103/PhysRevB.84.134433 PACS number(s): 75.10.Dg, 03.67.−a, 71.70.Ch, 76.30.Da

I. INTRODUCTION

Harmonic systems are a basic manifestation of quantum mechanics and appear in various forms, down to the nanoscale, as electromagnetic or mechanical oscillators. In the case of a finite number of excited states, multilevel systems are proposed to perform quantum algorithms in size-limited[1,2] or scalable[3] schemes by using microwave (MW) pulses to generate entangled states. The coherent manipulation of spins in a multilevel system is fundamental to the implementation of the Grover algorithm.[4] At the same time, the quasiharmonic nature of the system can lead to interesting effects, where the system behavior is tunable between a multi-level and a two-level type of system.[5]

Spin systems benefit from relatively large coherence and relaxation times, which makes them suitable as quantum-bit implementations or as a different type of quantum random access memory.[6–9] In some studies, the spin qubit operation is demonstrated at temperatures up to ambient.[10] Recent studies demonstrated that in diluted systems, spin-spin dipolar interactions are sufficiently low to allow coherent, quantum manipulations. Such situations are well exemplified by systems such as the nitrogen-vacancy color centers in diamonds,[11,12] N atoms in C_{60},[13] Er^{3+},[14,15] and Cr^{5+} (Ref. 16) ions and molecular magnets.[17,18]

In a previous work[5] we demonstrated multiphoton spin coherent manipulation in a multilevel system (Mn^{2+}) diluted in MgO, a highly symmetric nonmagnetic matrix. In this work we report on the possibility of using a multilevel system to tune the Rabi oscillations using a combination of two parameters: microwave power and/or magnetic-field orientation. To this end, one needs a magnetic system with a well-defined anisotropy, but sufficiently small in size to be overcome by microwave amplitudes achievable in typical experimental conditions.

The $S = 5/2$ Mn^{2+} spin is our system of choice. As detailed in Sec. II, the crystalline anisotropy for this high cubic symmetry is orders of magnitude smaller than the magnetic (Zeeman) energy and therefore the multilevel system is quasiharmonic. This is essential for successful multiphoton spin manipulation and for state tunability by magnetic-field orientation. At the same time, the anisotropy remains smaller than or comparable to the microwave drive, an aspect that is essential for tunability by drive.

In this $S = 5/2$ system we demonstrate multiphoton Rabi oscillations and controlled tuning of the system in and out of a quasiharmonic level configuration. Using the rotating-frame approximation, the experiments are explained very well by both an analytical model and a generalized numerical model. The calculated multiphoton Rabi frequencies and amplitudes are in excellent agreement with the experimental data.

The article is structured as follows. In Sec. II we describe the spin Hamiltonian and its parameters. In Sec. III the experimental procedure and setup are detailed. In Sec. IV an analytical and a numerical model are given, describing the tunability of the multiphoton dynamics. The experimental findings are described in Sec. V.

II. QUASIHARMONIC SPIN HAMILTONIAN

The spins $S = 5/2$ of the Mn^{2+} ions are diluted in a MgO nonmagnetic matrix of cubic symmetry $F_{m\bar{3}m}$ (lattice constant 4.216 Å). The Mn^{2+} ions are located in substitutional positions of Mg^{2+} ions. The high degree of symmetry ensures that the spins experience an almost isotropic crystalline environment and thus the fourth-order magnetic anisotropy can be made much smaller than the Zeeman splittings. Interactions between Mn^{2+} ions and symmetry deformations are neglected. The spin Hamiltonian at resonance is given by[19,20]

$$H = a/6\left[S_x^4 + S_y^4 + S_z^4 - S(S+1)(3S^2-1)/5\right] + \gamma \vec{H}_0 \cdot \vec{S} - A\vec{S}\cdot\vec{I} + \gamma \vec{h}_{\mathrm{MW}} \cdot \vec{S}\cos(2\pi f t), \quad (1)$$

where $\gamma = g\mu_B/h$ is the gyromagnetic ratio ($g = 2.0014$ is the g factor, μ_B is Bohr's magneton, and h is Planck's constant), $S_{x,y,z}$ are the spin projection operators, $\vec{S}$ is the total spin, $a = 55.7$ MHz is the anisotropy constant, $A = 244$ MHz is the hyperfine constant of ^{55}Mn ($I = 5/2$), h_{MW} and f represent the microwave amplitude and frequency, respectively,

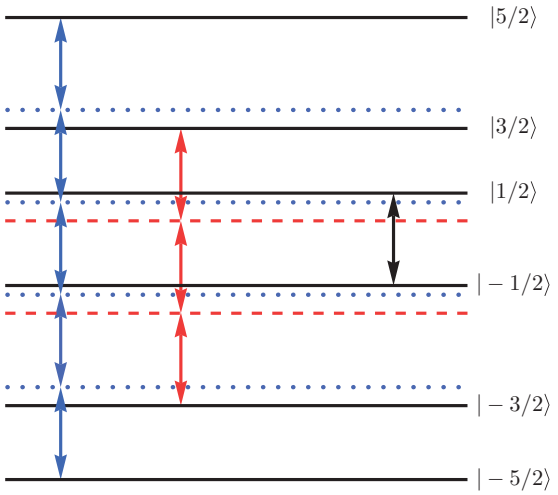

FIG. 1. (Color online) Level diagram of the Mn^{2+} spin in a cubic crystal field for a Zeeman splitting $\gamma H_0 = E_{1/2} - E_{-1/2}$. Arrows indicate one-photon (black), three-photon (red), and five- photon (blue) monochromatic transitions between spin projections m, as shown on the left-hand side. The dashed and dotted lines show equidistant virtual levels enhancing the multiphoton transitions.

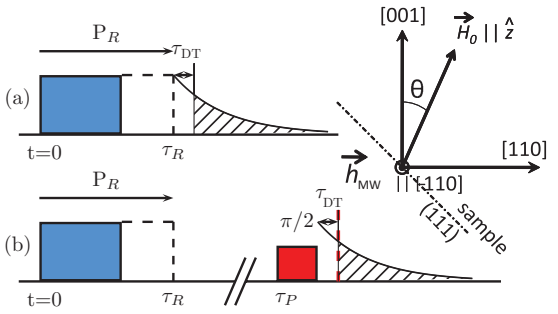

FIG. 2. (Color online) Pulse sequence used in the multiphoton Rabi oscillation measurements, which starts with a strong excitation pulse P_R inducing the multiphoton nutation. (a) Right after the pulse P_R, the free-induction-decay signal gives the transverse magnetization state between $-1/2$ and $1/2$. (b) After a time $\tau_P \gg T_2$, a $\pi/2$ pulse rotates the longitudinal magnetization so it can be measured by our setup (see the text for more details). The inset shows the static- and electromagnetic-field orientations with respect to the crystalline axes.

and $\vec{H}_0$ is the static field ($\vec{H}_0 \perp \vec{h}_{MW}$). In our experiments, the static field ensures a Zeeman splitting of $\gamma H_0 \approx f \sim 9$ GHz, which is much stronger than all other interactions of Eq. (1). This implies that (i) $\vec{H}_0$'s direction can be approximated as the quantization axis and (ii) coherent MW driving is confined between levels of the same nuclear spin projection m_I (see also Refs. 5, 21, and 22).

The six-level system is consequently quasiharmonic, as shown by the level diagram in Fig. 1. The dashed and dotted lines show virtual levels of equidistant separation $g\mu_B H_0 = hf$, which strongly enhance the multiphoton transition probabilities. Since $a \ll f$, the distance between the real and virtual levels in Fig. 1 is exaggerated for clarity. The number of arrows for each monochromatic transition suggests the type of multiphoton coherent excitation (one, three, or five photons). A coherent Rabi superposition of the $m = -5/2, \ldots, 5/2$ states (as counted on the left-hand side of the figure) can thus be obtained, which is strongly dependent on the microwave drive power and nutation time.

III. EXPERIMENTAL PROCEDURE

Rabi oscillation measurements have been performed in a Bruker Elexsys 680-pulse electron paramagnetic resonance (EPR) spectrometer working at about $f = 9.6$ GHz (X band). The sample is a $(3 \times 3 \times 1)$-mm^3 single crystal of MgO doped by a small amount of Mn^{2+} (a few parts per 10^6). The orientation between the sample and the static field is controlled by a goniometer (with a precision to 1°) with the rotation axis parallel to the MW magnetic-field direction $\vec{h}_{MW}$. In the measurements presented here, $\vec{h}_{MW}||[-110]$ (see Fig. 2 inset). All measurements have been made at room temperature. Calibration of the microwave field h_{MW} has been made using the 1,3-bisdiphenylene-2-phenylallyl (BDPA) standard: A small amount of BDPA containing isotropic $S = 1/2$ spins gives a Rabi frequency of exactly $F_R = \mu_B h_{MW}/h$.

By design, the detection is sensitive to frequency f and therefore it can probe only transitions between consecutive spin projections, $m \leftrightarrow m+1$. As the transition $|-1/2\rangle \leftrightarrow |1/2\rangle$ is of highest probability, as ensured by Fermi's golden rule, and is not sensitive to crystal strain effects we choose to use the levels $m = \pm 1/2$ as a probe of the six-level dynamics.

By definition, the magnetization is given by $\langle S_i \rangle \equiv \mathrm{Tr}(\rho S_i)$, where ρ is the density matrix and S_i is the $S = 5/2$ spin operator $i = x, y, z$. Since we probe only the transition $|-1/2\rangle \leftrightarrow |1/2\rangle$ we define the magnetization of the subset $\langle S_i \rangle_{1/2} \equiv \mathrm{Tr}(\rho_{1/2} S_i)$, where $\rho_{1/2}$ is the central block matrix of ρ corresponding to the base subset $|\pm 1/2\rangle$.

The drive and detection of the multiphoton Rabi oscillations are implemented with the pulse sequence presented in Fig. 2. A drive pulse P_R of duration τ_R and resonant to the $|-1/2\rangle \leftrightarrow |+1/2\rangle$ transition is applied at $t = 0$. At the end of this pulse, the density of states has been coherently changed.

Right after the P_R pulse, spin dephasing and line inhomogeneity induce a free induction decay (FID) signal.[23] The first point of this FID (at $t = \tau_R$) gives the transverse magnetization traced on the $|\pm 1/2\rangle$ subset: $\langle S_x \rangle_{1/2} = \rho_{-1/2,1/2} + \rho_{1/2,-1/2}$. Unfortunately, the dead time τ_{DT} of the spectrometer (~ 80 ns) prevents the measurement of this first point. If the entire inhomogeneous line $|-1/2\rangle \leftrightarrow |1/2\rangle$ of width ΔH_0 is excited by a sufficiently short P_R pulse (nonselective pulse, here $\tau_R^{-1} > \gamma \Delta H_0 / 2\pi = 0.27$ MHz), the FID is simply the Fourier transform of the absorption line and an exponential decay in MgO:Mn^{2+}. Therefore, we integrate the detected FID and the result is proportional to its first point. Note that for a broad line (not our case), as often seen in solid-state paramagnetic systems, the FID oscillates and the first point cannot be found so easily.[24,25]

The pulse sequence in Fig. 2(a) detects the coherent evolution of the transverse magnetization $\langle S_x \rangle_{1/2}$ as a function of pulse length τ_R. To probe the coherent evolution of the longitudinal magnetization $\langle S_z \rangle_{1/2} = \rho_{1/2,1/2} - \rho_{-1/2,-1/2}$ (also traced on the $|\pm 1/2\rangle$ subset), we use the sequence

shown in Fig. 2(b). After the Rabi pulse P_R, one waits a time $\tau_P - \tau_R$, which is smaller than the system's relaxation time T_1 but larger than the decoherence time T_2. Thus, at $t = \tau_P$, only the longitudinal magnetization is nonzero.[26]

A $\pi/2$ pulse follows, rotating the $|\pm 1/2\rangle$ population in a coherent mixture, which is located in the xy plane (or the equatorial plane). The detection observes the FID toward zero in this mixture, giving essential information such as the initial total magnetization in the xy plane, its FID decoherence time T_2^*, and a potential shift away from the resonance static field.

As indicated with arrows in Fig. 1, in a cubic symmetry the three- and five-photon transitions use the $|\pm 1/2\rangle$ states as intermediate ones. Therefore, the $\pi/2$ pulse can distinguish between the various multiphoton Rabi oscillations due to their different frequencies, as detailed in the following section.

IV. RABI ROTATIONS IN A TUNABLE MULTILEVEL SYSTEM: THEORETICAL TREATMENT

The aim of this section is to present a model that describes the coherent multiphoton Rabi oscillation that occurs in a quasiharmonic large spin system under monochromatic radiation. To compute the multiphoton Rabi frequencies, we used the density-matrix theory[27] applied to the Mn^{2+} ion ($S = 5/2, I = 5/2$) in the rotating-frame approximation.

A. Analytical calculation

Let us consider a quantum system with six states $|S_z\rangle$, $S_z = \{-5/2, -3/2, -1/2, 1/2, 3/2, 5/2\}$, irradiated by an electromagnetic field in resonance with the $-1/2$ and $1/2$ levels. We assume initially $I = 0$, but we will describe the effect of the nuclear spin at the end of this section. The Hamiltonian of the system is

$$\mathcal{H} = \hat{E} + \hat{V}(t) = \sum_{S_z=-5/2}^{5/2} E_{S_z} |S_z\rangle\langle S_z| + \hat{V}(t), \tag{2}$$

with E_{S_z} the static energy levels, $\hat{V}(t) = \frac{\gamma}{2} h_{\mathrm{MW}} (\hat{S}_+ + \hat{S}_-) \cos(2\pi f t)$, S_+ (S_-) the raising (lowering) operators, and $f = E_{1/2} - E_{-1/2}$.

In a cubic symmetry and first order in perturbation ($a \ll \gamma H_0$), the static energy levels are given by

$$\begin{aligned} E_{\pm 5/2} &= (\pm 5/2)\gamma H_0 + (1/2)pa + O(a^2), \\ E_{\pm 3/2} &= (\pm 3/2)\gamma H_0 - (3/2)pa + O(a^2), \\ E_{\pm 1/2} &= (\pm 1/2)\gamma H_0 + pa + O(a^2), \end{aligned} \tag{3}$$

where[19] $p = 1 - 5(A^2B^2 + B^2C^2 + C^2A^2)$, with A, B, and C representing the cosine directors of $\vec{H}_0$ with the crystalline axes. For our geometry, p is given by

$$p = 1 - 5\sin^2\theta + \frac{15}{4}\sin^4\theta, \tag{4}$$

with θ the angle between $\vec{H}_0$ and the c axis [001]. Since $H_0 \gg h_{\mathrm{MW}}$, we can use the rotating-wave approximation (RWA) to make Eq. (2) time independent. Since in a conventional pulsed spectrometer we have access to only the first harmonic detection hf, we define the unitary transformation

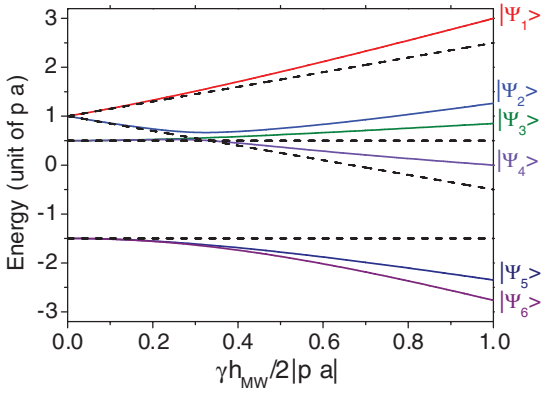

FIG. 3. (Color online) Eigenvalues of $\mathcal{H}_{\mathrm{RWA}}$ as a function of $\tilde{h}$. The dashed lines are the limit $h_{\mathrm{MW}} \ll pa$.

$U(t) = \exp(-i2\pi f \hat{S}_z t)$ and apply it to Eq. (2). In the rotating frame, the Hamiltonian in Eq. (2) becomes[21,28]

$$\begin{aligned} \mathcal{H}_{\mathrm{RWA}} &= U\mathcal{H}U^\dagger + i\hbar\frac{\partial U}{\partial t}U^\dagger \\ &= \begin{pmatrix} \frac{1}{2}pa & \frac{\sqrt{5}}{2}V & 0 & 0 & 0 & 0 \\ \frac{\sqrt{5}}{2}V & -\frac{3}{2}pa & \sqrt{2}V & 0 & 0 & 0 \\ 0 & \sqrt{2}V & pa & \frac{3}{2}V & 0 & 0 \\ 0 & 0 & \frac{3}{2}V & pa & \sqrt{2}V & 0 \\ 0 & 0 & 0 & \sqrt{2}V & -\frac{3}{2}pa & \frac{\sqrt{5}}{2}V \\ 0 & 0 & 0 & 0 & \frac{\sqrt{5}}{2}V & \frac{1}{2}pa \end{pmatrix}, \end{aligned} \tag{5}$$

where $V = \gamma h_{\mathrm{MW}}/2$. By diagonalization, the eigenenergies E_n/pa of the dressed states $|\Psi_n\rangle$ are calculated as a function of $\tilde{h} \equiv V/pa$, as illustrated in Fig. 3 (for $p > 0$).

For high anharmonicity or low microwave power $\tilde{h} \to 0$, in which case $|\Psi_1\rangle = (|1/2\rangle + |-1/2\rangle)/\sqrt{2}$ and $|\Psi_2\rangle = (|1/2\rangle - |-1/2\rangle)/\sqrt{2}$ are the coherent superposition of states $|\pm 1/2\rangle$. The other wave functions remain unchanged: $|\Psi_3\rangle = |5/2\rangle$, $|\Psi_4\rangle = |-5/2\rangle$, $|\Psi_5\rangle = |3/2\rangle$, and $|\Psi_6\rangle = |-3/2\rangle$. The splitting between $|\Psi_1\rangle$ and $|\Psi_2\rangle$ is detected as an oscillation of frequency $F_R = E_2 - E_1 = 3\frac{\gamma}{2}h_{\mathrm{MW}}$, in agreement with the general formula[22]

$$F_R^{(1)} = \frac{\gamma}{2}h_{\mathrm{MW}}\sqrt{S(S+1) - S_z(S_z+1)} \tag{6}$$

for one-photon Rabi oscillations between consecutive states S_z and $S_z + 1$.

When the microwave power h_{MW} increases, the degeneracy of $|\Psi_n\rangle$ ($n = 3,4,5,6$) is lifted, allowing coherent three- and five-photon transitions ($|-3/2\rangle \leftrightarrow |3/2\rangle$ and $|-5/2\rangle \leftrightarrow |5/2\rangle$, respectively). Note that two- and four-photon processes are out of resonance and therefore are not discussed here. In first-order perturbation in $\tilde{h}$, only the one-photon process exists between states $|\Psi_1\rangle$ and $|\Psi_2\rangle$. In third-order perturbation, a three-photon process mixes the states $|\pm 3/2\rangle$, leading to a pure three-photon Rabi oscillation with frequency $F_R^{(3)} = \frac{24}{25}\tilde{h}^3 pa$, as detailed in the Appendix. This three-photon

process perturbs the aforementioned one-photon process, which now has the Rabi frequency $F_R^{(1')} = F_R^{(1)} - \frac{24}{25}\tilde{h}^3 pa$.

In fifth-order perturbation, the five-photon process mixes the states $|\pm 5/2\rangle$, leading to a Rabi frequency $F_R^{(5)} = \frac{15}{2}\tilde{h}^5 pa$ (a pure five-photon process). Similarly, the five-photon process will change the dynamics of the three- and one-photon Rabi oscillations [see the Appendix, Eqs. (A3)–(A5)].

For $\tilde{h} \to \infty$, the microwave field excites all transitions and the six levels become equidistant [see Eq. (A7)] while the dynamics is coherently driven by a five-photon process. This dynamics resembles that of a spin $S = 1/2$. The diagonal of the Hamiltonian in Eq. (5) becomes negligible and the diagonalization simply rotates the Hamiltonian along the $h_{\rm MW}$ field.

When the nuclear spin is included, the model becomes more complicated, but analytical solutions can still be found. The full spin Hamiltonian of $^{55}Mn^{2+}$ $(S = 5/2, I = 5/2)$ is a 36×36 matrix. If we assume no forbidden nuclear transitions ($\Delta m_I = 0$, with m_I quantifying the I projections), the Hamiltonian in Eq. (1) can be separated into six 6×6 matrices of the form in Eq. (2).

The static energies E_{S_z} now depend also on m_I and A and have been computed in first-order perturbation in A/H_0 by Low.[19] Having the new E_{S_z} renormalized by the hyperfine field, we can use the same procedure as above to compute the eigenvalues of the dressed states and the Rabi splittings.

Finally, note that all other transitions can be computed by the method presented here by changing the value of f in Eq. (2). For instance, for $f = (E_{-3/2} - E_{1/2})/2$ one can study the two-photon Rabi oscillations in the transition $|-3/2\rangle \leftrightarrow |1/2\rangle$).

B. Numerical calculation

The analytical model presented above describes the multiphoton frequencies of the Rabi oscillations very well but fails to describe their intensities (the time evolution of spin populations). In order to describe the experimental results we developed a model using the Hamiltonian in Eq. (1), which shows the actual crystal-field parameters and includes the hyperfine coupling between the $S = 5/2$ electronic spin and the $I = 5/2$ nuclear spin of $^{55}Mn^{2+}$.

The anisotropy a and hyperfine A constants are two orders of magnitude smaller than the electron Zeeman interaction. Therefore, it is appropriate to assume that the orientation of the static field imposes the quantization axis $\tilde{z}$. On this basis, the Hamiltonian in Eq. (1) is rewritten as in Eq. (2), where E_{S_z} is obtained by exact diagonalization and reflects the hyperfine coupling.

Once we get the form of Eq. (2) for $\mathcal{H}$, the transformation into the rotating frame become obvious. Experimentally, the spectrometer signal represents the transient magnetic resonant signal in the rotating frame, obtained by mixing the signal reflected by the cavity $[S(t)\cos(2\pi f t)]$ and the reference arm $[\cos(2\pi f t)]$. This leads to a frequency-independent signal $S(t)$ and a double frequency signal (which is filtered out). The unitary transformation is fixed by the microwave frequency f, with $U(t) = \exp(-i2\pi \hat{S}_z f t)$, and using Eq. (5) one gets

$$\mathcal{H}_{\rm RWA} = \frac{\gamma}{2} h_{\rm MW} \hat{S}_x + \hat{E} - f\hat{S}_z. \tag{7}$$

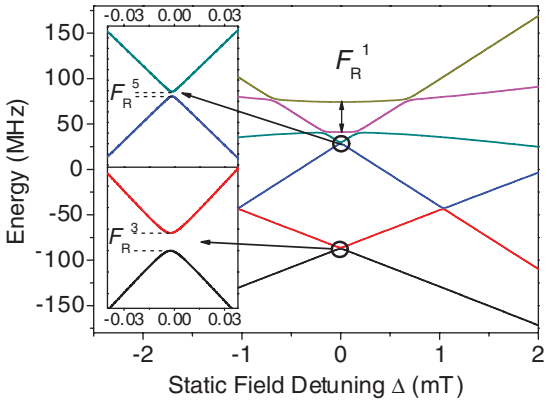

FIG. 4. (Color online) Dressed-state energies for $H_0||[100]$, $h_{\rm MW} = 0.8$ mT, and $m_I = 1/2$. The large anticrossing F_R^1 is the one-photon Rabi splitting. The insets are close-ups of the three-photon and five-photon Rabi splittings.

For a fixed m_I, the static field H_0 is chosen to satisfy the condition $E_{1/2} - E_{-1/2} + \Delta = f$, where Δ represents the detuning of the static field, away from resonance. As an example, the eigenvalues of the Hamiltonian in Eq. (7), for $H_0||[100]$ and nuclear projection $m_I = 1/2$, are shown in Fig. 4 as a function of field detuning Δ. In these simulations, $h_{\rm MW} = 0.8$ mT, which is sufficiently strong to induce Rabi splitting with three and five photons, as shown in insets.

The dynamics of the Hamiltonian in Eq. (7) is described by the time evolution of the 6×6 density matrix $\rho(t)$:

$$i\frac{d\rho}{dt} = [\mathcal{H}_{\rm RWA}, \rho]. \tag{8}$$

In the rotating frame (Dirac or interaction picture), the solution is $\rho(t) = U_p(t)\rho_0 U_p^\dagger(t)$, with ρ_0 the matrix density at thermal equilibrium,

$$\rho_0 = \frac{\exp(-\hat{E}/kT)}{\mathrm{Tr}[\exp(-\hat{E}/kT)]}, \tag{9}$$

and $U_p(t)$ is the propagator operator $U_p(t) = \exp(-i2\pi\mathcal{H}_{\rm RWA}t)$.

When the Rabi pulse P_R is applied, the spin population is coherently manipulated. At the end of the sequence a weak $\pi/2$ pulse will selectively probe the difference of population between states $-1/2$ and $1/2$. The signal out of the spectrometer is $S(t) = \sigma_{-1/2}(t) - \sigma_{1/2}(t)$. Note that for a spin $S = 1/2$, $S(t) = \langle S_z\rangle(t)$.

With the method presented here, the time evolution of $S(t)$ can be computed for a fixed value of the static H_0 and microwave $h_{\rm MW}$ fields. To extract the Rabi frequencies, we perform a fast Fourier transform (FFT) on the computed $S(t)$. Since the model does not take into account the decoherence or decay effects of the Rabi oscillations, we multiply the simulated $S(t)$ by a phenomenological exponential decay, with a characteristic time (or FFT width) similar to that of the experimentally observed oscillations.

V. EXPERIMENTAL RESULTS

A typical MW absorbtion spectrum of MgO:Mn^{2+} as a function of H_0 shows six sets (one for each m_I projection)

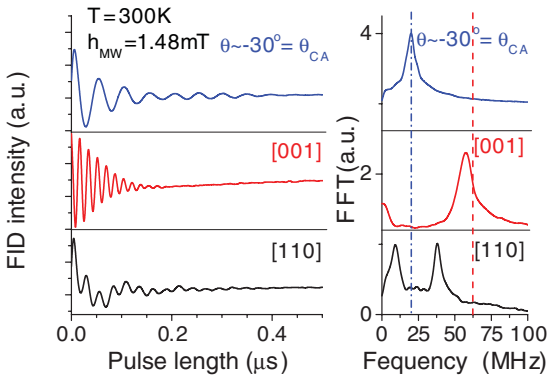

FIG. 5. (Color online) Rabi oscillation and its Fourier transforms for three H_0 orientations and for a microwave field $h_{\mathrm{MW}} = 1.48$ mT. For H_0 along the compensation angle (blue curves), the dynamics is the same as that of a $S = 1/2$ system. For $H_0||[001]$ (red curves) the microwave field is smaller than the effective anisotropy and only the one-photon process is induced. For $H_0||[110]$ (black curves) the microwave field and the effective anisotropy are comparable and the three-photon process becomes visible.

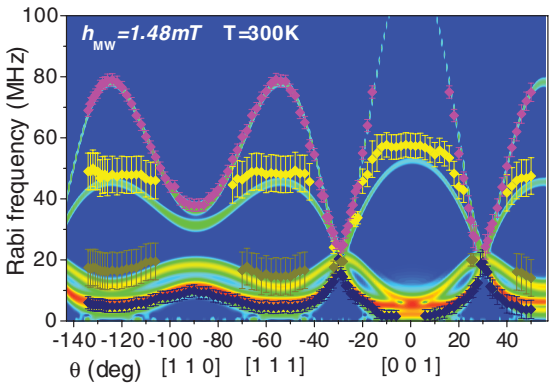

FIG. 6. (Color online) Rabi frequency distribution of MgO:Mn^{2+} while the static field H_0 rotates in the plane (-110) and for a microwave field $h_{\mathrm{MW}} = 1.48$ mT. The static field $H_0 = 348.5$ mT and frequency $f = 9.676$ GHz are set to probe the transition $|m_S = -1/2, m_I = 1/2\rangle \leftrightarrow |m_S = 1/2, m_I = 1/2\rangle$. The points represent peaks in the Fourier transform of the experimental data. The error bars are the width of the Fourier transform (consequence of the damping). The color plot is calculated with the numerical model given in Sec. IV B.

of five lines ($S_z \rightarrow S_z + 1, S_z = -5/2, \ldots, 3/2$). In the experiments described below, the magnetic field is tuned to study resonances in the set corresponding to $m_I = 1/2$. All experimental and theoretical results are valid for any other nuclear spin projection.

A. Tunable multiphoton Rabi oscillations by changing the orientation of the static field

The static-field orientation is described by the p parameter [see Eq. (4)] and therefore can tune the reduced microwave field $\tilde{h} = V/pa$. We measured Rabi oscillations and corresponding FFTs at constant microwave field (h_{MW}=1.48 mT) for three different orientations (and p values) of H_0, as shown in Fig. 5. One could see a highly anisotropic behavior of the coherent dynamics depending on the relative orientation between H_0 and the crystal axes.

For $H_0||[001]$ ($p = 1$, maximum value), only one frequency is observed, but its value (57 MHz) is smaller than the one expected for the one-photon Rabi frequency in the transition $-1/2 \leftrightarrow 1/2$ in $S = 5/2$ [62.5 MHz; see Eq. (6) and the red dashed line in Fig. 5]. Although the multiphoton Rabi oscillation is not clearly resolved, it is indirectly slowing down the expected one-photon dynamics, as described in Sec. IV A by the difference $F_R^{(1)} - F_R^{(1')} = F_R^{(3)}$.

For $H_0||[110]$ ($p = -1/4$), in addition to the high-frequency one-photon process, a low-frequency three-photon Rabi oscillation becomes observable due to a lower-p value and thus a larger $\tilde{h}$. Finally, for $\theta = \theta_{\mathrm{CA}}$ [the compensation angle of the cubic anisotropy: $p(\theta_{\mathrm{CA}}) = 0$] and hence $\tilde{h} \rightarrow \infty$, only one Rabi frequency is observed (Fig. 5, top). Its value is the same as the one expected for an isotropic spin (dash-dotted line in Fig. 5). As explained in Sec. IV A and the Appendix, a coherently driven five-photon process (and only this process) is induced, leading to a spin dynamics similar to that of a spin 1/2.

A detailed θ dependence of detected Rabi frequencies, defined as FFT peaks of coherent oscillations (as introduced in Fig. 5), is given in Fig. 6 for the same value of h_{MW}. The FFT peaks are shown by points. The error bars are FFT linewidths, which are due to decay processes in the Rabi oscillations. The contour plot is computed using the numerical model described in Sec. IV B, with no adjustable parameters: The crystal field and hyperfine constant are from Ref. 19 and the MW field has been independently calibrated using a standard. The agreement between our model and the experimental data is quite good; however, there are some discrepancies when $|pa|$ is small (but not zero) compared to $\gamma h_{\mathrm{MW}}/2$. In this case, the four EPR satellite lines are close to the central line and can overlap due to a small inhomogeneity caused by crystal-field strain. Since the multiphoton Rabi frequency is highly dependent on $|pa|$ (especially when $|pa|$ is small), the distribution in pa induces a high distribution of multiphoton Rabi frequencies, which in turn overdamps the Rabi oscillation signal.

B. Tunable multiphoton Rabi oscillations by changing the MW field

Aside from the tuning method based on static-field orientation, described in the preceding section, an alternative method is based on the MW drive intensity. To demonstrate the method, we apply a static field not far from the compensation angle θ_{CA} described above such that the spin system is slightly anisotropic. We choose an angle $\theta = 31 \pm 1^\circ$ and record coherent Rabi oscillations as a function of the microwave field h_{MW}. The FFT peaks (Rabi frequencies) are shown in Fig. 7 by points and the error bars represent the FFT linewidths. The dashed blue line is the MW field dependence of Rabi frequency for a pure one-photon transition between levels $|-1/2\rangle \leftrightarrow |1/2\rangle$ of the $S = 5/2$ system [$F_R = 3\frac{\gamma}{2} h_{\mathrm{MW}}$; see Eq. (6)]. The dotted black line is the MW field dependence of Rabi frequency in the case of a pure isotropic spin [$F_R = \frac{\gamma}{2} h_{\mathrm{MW}}$; see Eq. (A7)].

Indeed, at low MW power, the system has the dynamics of an anisotropic $S = 5/2$ system, as shown by the very

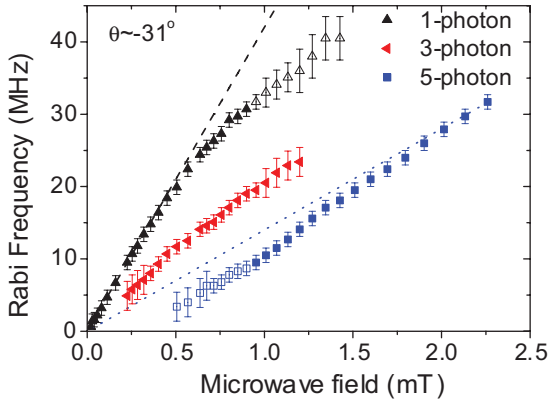

FIG. 7. (Color online) Rabi frequencies of the Mn^{2+} spin, as a function of drive field, obtained by a FFT of the detected coherent oscillations. The error bars are the FFT linewidths. The solid (open) colored symbols correspond to high- (low-) intensity signals. The dashed line indicates the expected one-photon dependence given by Eq. (6), whereas the dotted line models the isotropic $S = \frac{5}{2}$ case [see Eq. (A7)].

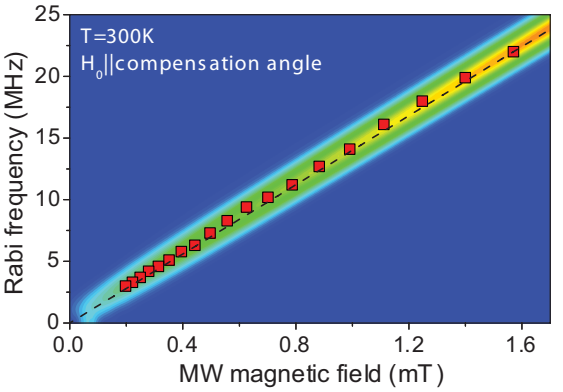

FIG. 8. (Color online) Rabi frequencies as FFT peaks (solid squares) of coherent oscillations for H_0 along the compensation direction of the cubic anisotropy $\theta = \theta_{CA}$. The color plot is numerically computed, as described in Sec. IV B, while the dashed line shows the expected behavior for an isotropic $S = 5/2$ system [see Eq. (A7)].

good agreement between experimental points (up-pointing triangles) and the expected dependence for a one-photon process (dashed line). At intermediate powers, the FFT clearly shows the existence of a three-photon process (left-pointing triangles) as well as a five-photon process. The latter is indicated by open squares for shallow peaks in the FFT and by solid squares corresponding to well-defined FFT peaks. The low-h_{MW} behavior of the three- and five-photon processes is nonlinear, as described by Eqs. (A4) and (A5).

A quantitative numerical description is quite difficult because of the extreme nonlinearity of $\tilde{h}$ near θ_{CA}. At the compensation angle ($\theta_{CA} = 29.67°$) $\tilde{h} \to \infty$, but a small change in θ induces significant changes in $\tilde{h}$ (e.g., at $\theta = 30°$, $\tilde{h} = 16.3h_{MW}$; at $\theta = 31°$, $\tilde{h} = 4.1h_{MW}$; and at $\theta = 32°$, $\tilde{h} = 2.4h_{MW}$). As the accuracy of our goniometer is 1°, a numerical quantitative description around θ_{CA} is not relevant. Qualitatively, one notes that for $h_{MW} > 0.5$ mT, the one-photon Rabi frequency deviates from $F_R^{(1)}$ of Eq. (6) due to the formation of multiphoton processes. For high microwave powers ($h_{MW} > 1$ mT), the one-photon FFT peak is barely visible (shown by open up-pointing triangles) while the five-photon process entirely dominates the dynamics. This is indicated by the good agreement between the five-photon FFT peaks (solid squares) and the dotted line resulting from an isotropic $S = 5/2$ model (or a spin 1/2), as explained by Eq. (A7).

Our experiment demonstrates that a sufficiently intense microwave field can tune the spin dynamics from that of an anisotropic (unequidistant) system to that of an equidistant, quasiharmonic five-level system (equivalent to a two-level system).

C. Five-photon Rabi oscillations at the compensation angle

When the static field is applied along a direction for which $\theta = \theta_{CA}$ (that is, $\theta = 29.67°$), the cubic anisotropy is geometrically compensated for and therefore $p = 0$ and $\tilde{h} \to \infty$. As explained in Sec. IV A and the Appendix, one expects a perfectly isotropic $S = 5/2$ spin system.

We performed room-temperature Rabi oscillations for this field orientation. The FFT of the coherent oscillations are single peaked, as shown in Fig. 8 with solid squares (the FFT width is smaller than the size of the symbol). The color plot is calculated using the numerical procedure described in Sec. IV B and the dashed line indicates the analytical result of Eq. (A7). There is excellent agreement between the analytical and numerical models and the experimental data points (no fit parameter has been used).

During a Rabi rotation for this isotropic case, the spin density gradually moves upward on the equidistant six-level ladder and when it reaches the highest level ($S_z = 5/2$), the dynamics is reversed. In contrast to a one-photon dynamics, here we have a collective five-photon process, ensuring a continuous nutation within the $S_z = -5/2, \ldots, 5/2$ space.

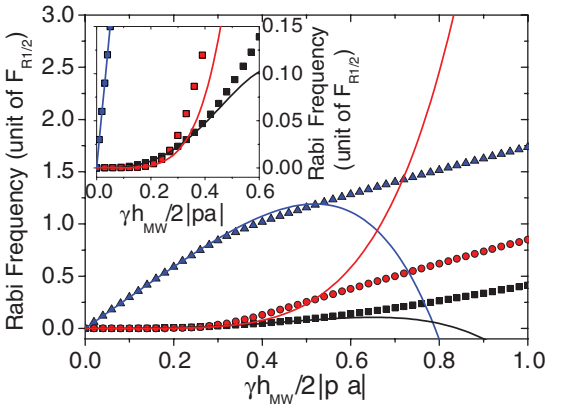

FIG. 9. (Color online) Rabi frequency dependence as a function of the reduced MW field $\tilde{h}$. Data points are numerically computed by solving Eq. (A1), while lines are the analytical perturbation developments [Eqs. (A3)–(A5)]. The inset shows a close-up at low fields and low Rabi frequencies.

VI. DISCUSSION

The experimental data and the model presented here use a monochromatic source to both induce and probe the multiphoton Rabi oscillations. Therefore, we restrict the types of multiphoton transitions that are measurable to those that exist at the same resonant static field as the one-photon transition (used to induce and probe). In order to probe directly all types of multiphoton transitions, two tunable frequencies will be needed: one to induce the multiphoton oscillations, i.e., to induce a two-photon Rabi oscillation [$f_1 = (E_{1/2} - E_{-3/2})/2$], and one to probe it ($f_2 = E_{1/2} - E_{-1/2}$). Note that the experiments described here, with a single or two tunable frequencies, have the appeal of being applicable to on-chip studies, using detectors placed in strong magnetic fields.[29–31]

VII. CONCLUSION

We report on single-photon and multiphoton coherent rotations in a $S = 5/2$ spin system featuring a cubic anisotropy. The anisotropy is much smaller than the Zeeman splittings, i.e., the six-level scheme shows only a small deviation from an equidistant diagram. This allows us to tune the spin dynamics by compensating for the cubic anisotropy with either a precise static-field orientation or a microwave-field intensity. In both cases, we can transition the system between an anisotropic to an isotropic situation, the latter case showing a spin dynamics corresponding to a two-level system. The experimental data are explained well by both theoretical and numerical models.

ACKNOWLEDGMENTS

This work was supported by City of Marseille, Aix-Marseille University (BQR grant), NSF Cooperative Agreement Grant No. DMR-0654118, NSF Grant No. DMR-0645408, and the Sloan Foundation. We thank A. Verga for fruitful discussion and G. Gerbaud (BIP-UPR9036) and the multidisciplinary EPR facility of Marseille (PFM Saint Charles) for technical support.

APPENDIX: EIGENVALUES OF DRESSED STATES

Diagonalization of the Hamiltonian in Eq. (5) can be achieved analytically. Since the most relevant parameter is the value of the microwave field compared to the anharmonicity parameter pa, we define the reduced field $\tilde{h} = \gamma h_{\mathrm{MW}}/2pa$. The eigenvalues of Eq. (5) are the solutions of the polynomial equations

$$\mathcal{P}_{\pm} = 6 \pm 9\tilde{h} + 18\tilde{h}^2 \pm 15\tilde{h}^3 + \cdots + (-14 \mp 12\tilde{h} - 26\tilde{h}^2)\mathcal{E} \mp 12\tilde{h}\mathcal{E}^2 + 8\mathcal{E}^3 = 0. \quad \text{(A1)}$$

For $\tilde{h} \to 0$, in first-order perturbation, Eq. (A1) becomes

$$\mathcal{P}_{\pm} \approx 6 \pm 9\tilde{h} + (-14 \mp 12\tilde{h})\mathcal{E} \mp 12\tilde{h}\mathcal{E}^2 + 8\mathcal{E}^3 = 0, \quad \text{(A2)}$$

with solutions $\mathcal{E}_{1,2} = 1 \pm 1.5\tilde{h}$, $\mathcal{E}_{3,4} = 0.5$, and $\mathcal{E}_{5,6} = -1.5$. The RWA wave functions are now $|\Psi_1\rangle = (|1/2\rangle + |-1/2\rangle)/\sqrt{2}$, $|\Psi_2\rangle = (|1/2\rangle - |-1/2\rangle)/\sqrt{2}$, $|\Psi_3\rangle = |5/2\rangle$, $|\Psi_4\rangle = |-5/2\rangle$, $|\Psi_5\rangle = |3/2\rangle$, and $|\Psi_6\rangle = |-3/2\rangle$. Rabi oscillations occur only between states $|\Psi_1\rangle$ and $|\Psi_2\rangle$ with frequency $F_R^1 = (\mathcal{E}_1 - \mathcal{E}_2)pa$ [see Eq. (6)]. We found the classical result that during the resonance $|1/2\rangle$ and $|-1/2\rangle$ are mixed by the electromagnetic wave and the other states stay unperturbed.

When $\tilde{h}$ is increased, we computed the solutions of Eq. (A1) up to the fifth-order perturbation in $\tilde{h}$. The Rabi frequencies $F_R = (\mathcal{E}_+ - \mathcal{E}_-)|pa|$ are

$$F_R^1 = pa\left(3\tilde{h} - \frac{24\tilde{h}^3}{25} - \frac{768\tilde{h}^5}{125}\right), \quad \text{(A3)}$$

$$F_R^3 = pa\left(\frac{24\tilde{h}^3}{25} - \frac{339\tilde{h}^5}{250}\right), \quad \text{(A4)}$$

$$F_R^5 = pa\left(\frac{15\tilde{h}^5}{2}\right). \quad \text{(A5)}$$

These equations are used to simulate the solid lines in Fig. 9, which are compared to the numerical solutions of Eq. (A1) (discrete data points). The inset shows a close-up view at low microwave powers and Rabi frequencies. One could conclude that for powers up to $\tilde{h} \sim 1/2$, the perturbative analysis works very well.

When $\tilde{h} \to \infty$, Eq. (A1) becomes

$$\mathcal{P}_{\pm} \approx \pm 15\tilde{h}^3 - 26\tilde{h}^2\mathcal{E} \mp 12\tilde{h}\mathcal{E}^2 + 8\mathcal{E}^3 = 0, \quad \text{(A6)}$$

with solutions $\mathcal{E}_{\pm} = \tilde{h}[\pm\frac{1}{2}; \mp\frac{3}{2}; \pm\frac{5}{2}]$, which represent dressed-state energies of an isotropic spin 5/2 with Rabi frequency:

$$F_{5/2}^{\mathrm{iso}} = F_{1/2} = \frac{\gamma}{2}h_{\mathrm{MW}}. \quad \text{(A7)}$$

*sylvain.bertaina@im2np.fr
†Present address: Materials Science Division, Argonne National Laboratory, 9700 S. Cass Avenue, IL 60439, USA.
‡ic@magnet.fsu.edu

[1] M. N. Leuenberger and D. Loss, Nature (London) **410**, 789 (2001).
[2] M. N. Leuenberger, D. Loss, M. Poggio, and D. D. Awschalom, Phys. Rev. Lett. **89**, 1 (2002).
[3] M. Grace, C. Brif, H. Rabitz, I. Walmsley, R. Kosut, and D. Lidar, New J. Phys. **8**, 35 (2006).
[4] L. Grover, Phys. Rev. Lett. **79**, 325 (1997).
[5] S. Bertaina, L. Chen, N. Groll, J. Van Tol, N. S. Dalal, and I. Chiorescu, Phys. Rev. Lett. **102**, 50501 (2009).
[6] M. Blencowe, Nature (London) **468**, 44 (2010).
[7] I. Chiorescu, N. Groll, S. Bertaina, T. Mori, and S. Miyashita, Phys. Rev. B **82**, 024413 (2010).
[8] Y. Kubo, F. Ong, P. Bertet, D. Vion, V. Jacques, D. Zheng, A. Dréau, J.-F. Roch, A. Auffeves, F. Jelezko, J. Wrachtrup, M. Barthe, P. Bergonzo, and D. Esteve, Phys. Rev. Lett. **105**, 1 (2010).

[9]D. Schuster, A. Sears, E. Ginossar, L. DiCarlo, L. Frunzio, J. Morton, H. Wu, G. Briggs, B. Buckley, D. Awschalom, and R. Schoelkopf, Phys. Rev. Lett. **105**, 020504 (2010).
[10]A. V. Akimov, A. Mukherjee, C. L. Yu, D. E. Chang, A. S. Zibrov, P. R. Hemmer, H. Park, and M. D. Lukin, Nature (London) **450**, 402 (2007).
[11]M. V. G. Dutt, L. Childress, L. Jiang, E. Togan, J. Maze, F. Jelezko, A. S. Zibrov, P. R. Hemmer, and M. D. Lukin, Science **316**, 1312 (2007).
[12]R. Hanson, V. V. Dobrovitski, A. E. Feiguin, O. Gywat, and D. D. Awschalom, Science **320**, 352 (2008).
[13]G. Morley, J. van Tol, A. Ardavan, K. Porfyrakis, J. Zhang, and G. Briggs, Phys. Rev. Lett. **98**, 220501 (2007).
[14]S. Bertaina, S. Gambarelli, A. Tkachuk, I. N. Kurkin, B. Z. Malkin, A. Stepanov, and B. Barbara, Nature Nanotechnol. **2**, 39 (2007).
[15]S. Bertaina, J. H. Shim, S. Gambarelli, B. Z. Malkin, and B. Barbara, Phys. Rev. Lett. **103**, 226402 (2009).
[16]S. Nellutla, K.-Y. Choi, M. Pati, J. van Tol, I. Chiorescu, and N. S. Dalal, Phys. Rev. Lett. **99**, 137601 (2007).
[17]S. Bertaina, S. Gambarelli, T. Mitra, B. Tsukerblat, A. Müller, and B. Barbara, Nature (London) **453**, 203 (2008).
[18]S. Takahashi, J. van Tol, C. C. Beedle, D. N. Hendrickson, L.-C. Brunel, and M. S. Sherwin, Phys. Rev. Lett. **102**, 087603 (2009).
[19]W. Low, Phys. Rev. **105**, 793 (1957).
[20]S. Smith, P. Auzins, and J. Wertz, Phys. Rev. **166**, 222 (1968).
[21]C. Hicke and M. Dykman, Phys. Rev. B **76**, 54436 (2007).
[22]A. Schweiger and G. Jeschke, *Principles of Pulse Electron Paramagnetic Resonance* (Oxford University Press, New York, 2001).
[23]F. Bloch, Phys. Rev. **70**, 460 (1946).
[24]M. Kunitomo, T. Endo, S. Nakanishi, and T. Hashi, Phys. Rev. A **25**, 2235 (1982).
[25]A. Schenzle, N. Wong, and R. Brewer, Phys. Rev. A **21**, 887 (1980).
[26]S. Stoll, J. Magn. Reson. **130**, 86 (1998).
[27]R. Brewer and E. Hahn, Phys. Rev. A **11**, 1641 (1975).
[28]M. N. Leuenberger and D. Loss, Phys. Rev. B **68**, 165317 (2003).
[29]L. Chen, W. Wernsdorfer, C. Lampropoulos, G. Christou, and I. Chiorescu, Nanotechnology **21**, 405504 (2010).
[30]N. Groll, S. Bertaina, M. Pati, N. S. Dalal, and I. Chiorescu, J. Appl. Phys. **106**, 046106 (2009).
[31]N. Groll, A. Gurevich, and I. Chiorescu, Phys. Rev. B **81**, 020504 (2010).